

Additional Topics on Inertial Sensors and Inertial Navigation

Paul D. Groves

E.1	New Inertial Sensor Technology	E-1
E.1.1	Time-domain Switching Accelerometers	E-1
E.1.2	Cold-Atom Interferometry	E-2
E.2	Spinning-Mass Gyroscopes	E-3
E.2.1	Angular Rate Sensing	E-3
E.2.2	Error Characteristics	E-5
E.2.3	Aircraft Directional Gyro	E-5
E.3	All-Accelerometer IMUs	E-6
E.4	History of Inertial Navigation	E-7
E.5	Platform INS	E-7
E.6	Quaternion Navigation Equations Implementation	E-8
E.6.1	Quaternion Algebra	E-9
E.6.2	Attitude, Rotation, and Resolving Axes Transformations	E-11
E.6.3	Attitude Update	E-12
E.7	Local Tangent-Plane Frame Navigation Equations	E-14
E.8	Navigation Equations Iteration Rate Issues	E-15
E.9	Effects of Timing Errors	E-16
E.10	Pseudo-measurement Generation using Motion Constraints	E-16
	References	E-18

This appendix presents some additional topics on the subject of inertial sensors and inertial navigation. Section E.1 discusses time-domain switching accelerometers and cold-atom interferometry. Section E.2 describes spinning mass gyroscopes, including the aircraft directional gyro. Section E.3 explains the principles of the all-accelerometer IMU.

Section E.4 then presents some brief notes on the history of inertial navigation. Section E.5 describes the platform INS. Section E.6 describes navigation equations using the quaternion attitude representation instead of coordinate transformation matrices. Section E.7 describes a local tangent-plane implementation of the navigation equations. Section E.8 discusses a number of navigation equations iteration rate issues, including using different iteration rates for different stages of processing, using numerical integration, and iterating approximate forms of the navigation equations faster than the IMU output rate. Section E.9 discusses the effects of timing errors on inertial navigation. Finally, Section E.10 describes the generation of roll- and pitch axis angular rate pseudo-range measurements using land vehicle motion constraints.

E.1 New Inertial Sensor Technology

This section describes the time-domain switching (TDS) accelerometer and cold-atom interferometry.

E.1.1 Time-domain Switching Accelerometers

The time-domain switching (TDS) accelerometer is a new MEMS technology under development at the time of writing [1]. The proof mass of a TDS accelerometer is made to oscillate continuously along the sensitive axis at a frequency between 1 kHz and 10 kHz.

When a specific force is applied to the accelerometer along its sensitive axis, the mid-point and limits of the proof-mass oscillation are shifted with respect to the case in the same way as in a conventional pendulous accelerometer.

Instead of measuring the absolute position of the proof mass, a TDS accelerometer times the proof mass's crossing of two thresholds at equal distances either side of the equilibrium point. This provides two time intervals: the time spent above the upper threshold, τ_u , and the time spent below the lower threshold, τ_l . Where no specific force is applied, these two time intervals will be approximately equal; otherwise, they will be different, as shown in Figure E.1. The specific force may thus be calculated as a function of τ_u and τ_l , the oscillator period and amplitude, and the detector positions.

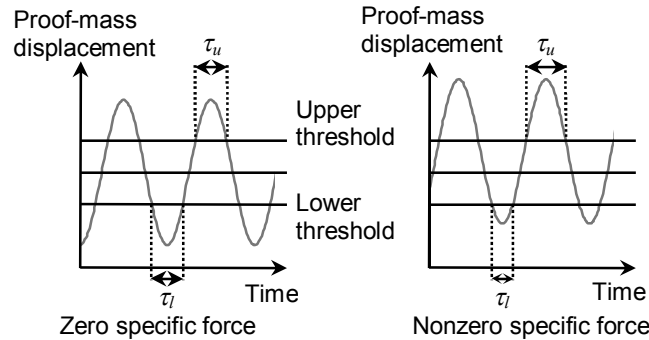


Figure E.1 Timing of proof-mass motion in a TDS accelerometer.

It is claimed that a TDS accelerometer can operate with higher accuracy and lower noise than conventional MEMS accelerometers because time can be measured with a greater precision than displacement [1]. However, the technology was still under development at the time of writing.

E.1.2 Cold-Atom Interferometry

A cold-atom inertial sensor operates in a pulsed mode. A magneto-optic trap and laser cooling technology is used to generate a cloud of cold atoms. This is then released from the trap into an evacuated chamber containing an atom interferometer. When the instrument is stationary, the atoms fall due to the gravitational force. By using the interferometer to measure the motion of the atoms with respect to the instrument, the specific force and/or the angular rate of the instrument is obtained with respect to inertial space. Instead of using a separate sensor for each degree of freedom, all measurements are made on the same cloud of cold atoms. Which quantities are measured depends on the configuration of the interferometers within the instrument [2–6].

At the time of writing, the technology was small enough for deployment on larger submarines, ships, and large aircraft, but too big for smaller vehicles (or pedestrians).

Cold-atom inertial sensors are much more precise than other technologies. The specific-force measurement noise is less than $1.1 \text{ ng}/\sqrt{\text{Hz}}$ ($1.1 \times 10^{-8} \text{ m s}^{-1.5}$) [6] and the angular-rate measurement noise is $8.5 \times 10^{-8} \text{ rad s}^{-0.5}$ or $2.95 \times 10^{-4} \text{ }^\circ/\sqrt{\text{hr}}$ [3]. However, early instruments were limited by their duty cycles, with pulsing rates less than 10 Hz. As the specific force and angular rate are only measured during part of the duty cycle, this is insufficient to capture the host-vehicle motion properly. One solution to this problem is to operate several inertial sensors in parallel with interleaved duty cycles [2]. This would obviously increase the cost, size, and power consumption. However, the latest sensors can measure specific force at a rate of up to 330 Hz [4], which is comparable with conventional inertial sensors.

Note that combining cold-atom interferometry with conventional inertial sensors would lose the benefit of the atom interferometer's very low noise levels.

The gravity gradient may also be measured using atom interferometry. A low duty cycle does not present a problem for this provided the instrument is mounted on a stabilized

platform, aligned with north, east, and down. Consequently, gravity gradiometry is the first navigation application of cold-atom interferometry [6].

E.2 Spinning-Mass Gyroscopes

This section describes the spinning mass gyroscope, including how it senses angular rate and its error characteristics. The definition of a gyroscope was originally synonymous with the spinning-mass type, but now encompasses all angular-rate sensors that do not require an external reference. Jean Bernard Léon Foucault is credited with inventing the spinning-mass gyro in 1852, whilst Charles Stark Draper led the development of high-performance gyros of this type in the 1950s [7].

For angular rate measurement, spinning-mass gyros have been superseded by optical and vibratory technology and are found principally in legacy equipment. However, absolute attitude sensors based on spinning-mass gyro technology are still available. The marine gyrocompass is described in Section 6.1.2 and the aircraft directional gyro in Section E.2.3 of this appendix. Gyroscopes for angular rate measurement are sometimes known as rate gyros to distinguish them from absolute attitude sensors.

E.2.1 Angular Rate Sensing

Spinning-mass gyros operate on the principle of conservation of angular momentum. Part of Newton's second law of dynamics, this states that the angular momentum of a body with respect to inertial space will remain unchanged unless acted upon by a torque (force \times distance). Therefore, if a spinning mass is mounted in an instrument case such that it is free to rotate about both of the axes perpendicular to its spin axis, it will remain aligned with respect to inertial space as the case is rotated. Pickoffs that measure the orientation of the spinning mass with respect to the case thus provide measurements of the instrument case's attitude about two axes. The resolution of attitude pickoffs limits the usefulness of these free gyros for inertial navigation. However, this configuration forms the basis of both the marine gyrocompass and the aircraft directional gyro, which are used as stand-alone attitude sensors.

For strapdown inertial navigation, a spinning-mass gyro must measure the angular rate about an axis which is fixed with respect to the instrument case. Figure E.2 shows a disc spinning about the y -axis with angular momentum vector \mathbf{h} . A torque, $\boldsymbol{\tau}$, is applied about the orthogonal z -axis. Consider the elements of the disc furthest away from the z -axis at the top and bottom of the diagram. As a result of the disc's spinning, these elements have a velocity of $\pm v_s$ along the z -axis. However, integrating the torque about the z -axis also gives these elements a velocity of $\mp v_t$ along the y -axis, changing their trajectory. Extending this to every element of the disc causes it to rotate about the x -axis, mutually perpendicular to both the spin and torque axes. This motion about the x -axis is known as precession.

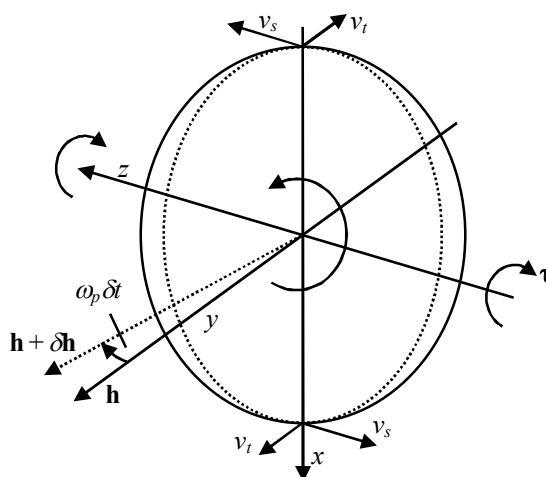


Figure E.2 Effect of orthogonal torque on a spinning disc.

Consider a small precession through an angle $\omega_p \delta t$ where ω_p is the precession angular rate and δt is a time increment. The resulting change in the angular momentum vector, $\delta \mathbf{h}$, is proportional to the magnitude of the original angular momentum \mathbf{h} and the precession angle $\omega_p \delta t$, but is mutually perpendicular. Thus,

$$\delta \mathbf{h} = \boldsymbol{\omega}_p \wedge \mathbf{h} \delta t. \quad (\text{E.1})$$

The applied torque is equal to the rate of change of angular momentum, so

$$\boldsymbol{\tau} = \boldsymbol{\omega}_p \wedge \mathbf{h}. \quad (\text{E.2})$$

Applying this to a spinning-mass gyro, if the case is rotated about an axis perpendicular to the spin axis, a torque about the mutually perpendicular axis must be applied to the spinning mass to keep it aligned with the case.

Figure E.3 shows an open-loop single-degree-of-freedom spinning-mass gyro. The spinning mass or rotor and its driving motor are mounted on a pivot about which the motor/rotor assembly is free to move. This axis is known as the output axis. The axis that is mutually perpendicular to the output and spin axes is known as the input axis, the axis about which the gyro measures rotation. The motor/rotor assembly cannot move about the input axis with respect to the case. When the gyro case is rotated about the input axis, it applies torque about that axis to the rotor, causing rotation about the output axis. With no reaction to this, the motor/rotor assembly would precess until the spin and input axes are aligned. One or more springs are mounted between the case and the motor. These springs provide a balancing torque about the output axis, which precesses the rotor about the input axis, keeping it aligned with the casing. Alternatively, the output-axis pivot can be replaced by a torsion bar. Thus, the input and output axes act both as torquing and precession axes with the torques applied by the case about the input axis balanced by the torque applied by the springs about the output axis. The force applied by a spring is a function of its compression or tension. Consequently, when rotation is applied about the input axis, the motor/rotor assembly will rotate about the output axis until the torques balance. The orientation of the motor/rotor assembly with respect to the case is proportional to the angular rate about the input axis. Thus, a pickoff provides an angular rate measurement.

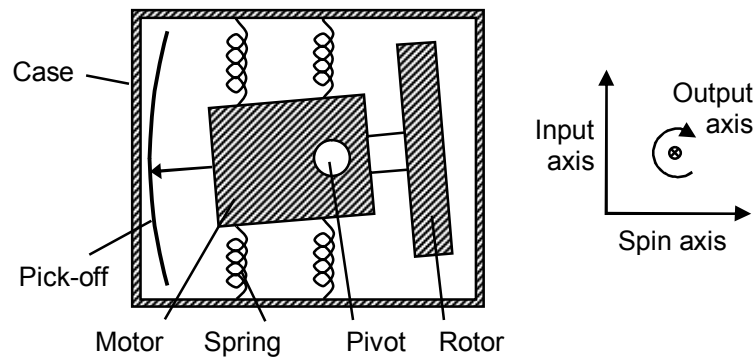


Figure E.3 Open-loop single-degree-of-freedom spinning-mass gyro.

When the case is rotated about the output axis, the springs are compressed or stretched, changing the torque about this axis and stimulating precession about the input axis. The case then prevents the precession about the input axis by applying an opposing torque which precesses the motor/rotor assembly about the output axis such that it retains a constant orientation with respect to the casing. Hence, only rotation about the input axis produces a reading.

The open-loop spinning-mass gyro suffers from the same limitations as the open-loop pendulous accelerometer (Section 4.1.1). The pickoff resolution is limited, the spring exhibits nonlinearity and hysteresis, and the orientation of the input axis with respect to the instrument casing varies. The solution is closed-loop operation. This replaces the springs with an

electromagnetic torquer. A capacitive, inductive or optical pickoff is used to detect misalignment of the motor/rotor assembly with respect to the gyro case and adjust the torquer to compensate. The torque exerted by the torquer is proportional to the angular rate of the gyro case about the input axis. Maximum sensitivity is obtained by maximizing the angular momentum of the spinning mass; this can be done by concentrating most of the rotor's mass around its edge. Different gyro performances can be offered at different prices by varying the quality of the spin motor, bearings, torquer, control electronics, and the size and symmetry of the rotor. The maximum angular rate that a spinning mass gyro can measure is between 5 and 15 rad s^{-1} [8].

Spinning-mass gyros may also be designed to sense rotation about two orthogonal axes; these are known as two-degrees-of-freedom gyros. The simplest approach is to mount a single-degree-of-freedom gyro on a gimbal frame that is attached to the gyro case by pivots on an orthogonal axis to the pivots supporting the rotor/motor assembly. An additional torquer and pickoff are then mounted between the gimbal frame and the gyro case. This is essentially one single-degree-of-freedom gyro inside another with the input and output axes of the “two gyros” exchanged. Other approaches include gyros with a floated spherical rotor and the dynamically tuned gyro, where the rotor is attached to the spin motor by a universal joint [8, 9]. For applications requiring angular-rate measurement about only two axes, a two-degrees-of-freedom gyro can be cheaper than two single-degree-of-freedom sensors.

E.2.2 Error Characteristics

The different error sources exhibited by inertial sensors are introduced in Section 4.4. Here, the error characteristics of spinning-mass gyros are summarized. The biases of spinning-mass gyros span the whole performance range from 0.001 to 100 $^{\circ} \text{hr}^{-1}$. The scale factor and cross-coupling errors are between 10^{-4} and 10^{-3} (100–1000 ppm). Spinning-mass gyros exhibit low random noise with a root PSD of 0.002 $^{\circ}/\sqrt{\text{hr}}$ typical of aviation-grade gyros; this is mainly due to mechanical instabilities.

Spinning-mass gyros exhibit a sensitivity to specific force due to mass unbalance. The coefficient of this g-dependent bias is around 1–10 $^{\circ}/\text{hr/g}$ and the gyros can be sensitive to accelerations along all three axes. Spinning-mass gyros can also exhibit anisoelastic or g^2 -dependent biases, which are proportional to the products of accelerations along pairs of orthogonal axes; anisoertia errors, which are proportional to the products of angular rate about pairs of orthogonal axes; and sensitivity to angular acceleration due to the inertia of the rotor [8].

E.2.3 Aircraft Directional Gyro

A directional gyro is used to aid aircraft heading determination in light aircraft [10]. It is used within the cockpit display rather than as part of an integrated navigation system. It typically costs between \$500 and \$2,000 or €400 and €1,600. It consists of a spinning-mass gyro mounted inside a frame, known as a gimbal, that is free to rotate about the body-frame z -axis. The gyro's spin axis thus remains within the body-frame xy -plane. The gimbal and spin axis are thus in the horizontal plane when the aircraft is level. Conservation of angular momentum keeps the spin axis aligned with respect to inertial space. After initial alignment, reading off the direction of the gyro's spin axis within the gimbal thus gives the aircraft's heading when it is level. This heading reading is in error when the aircraft pitches or rolls, but recovers when it levels off.

Basic directional gyros are physically mounted within the cockpit display and are pneumatically driven, spinning via suction from a vacuum pump driven by the aircraft's engine. Higher-performance models are electrically powered.

The direction of the gyros's spin axis will drift with time due to instrument errors, while the orientation of the north-south axis in the horizontal plane with respect to inertial space varies as the Earth rotates and the aircraft moves. In basic models, this must be periodically corrected by the pilot, making use of the magnetic compass reading. In more expensive models, a second gimbal, mounted inside the read-out gimbal with its axis mutually

perpendicular to the spin axis and the other gimbal, is used to apply torque to rotate the spin axis within the xy plane to keep it aligned with north-south (or east-west). The control signal for the torquer may be obtained by comparing the heading reading with a magnetic compass when the aircraft is level. Alternatively, it may be calculated as a function of position and velocity to compensate the rotation of the local navigation frame with respect to inertial space, leaving the instrument errors uncompensated. In this latter case, better quality gyros, with 0.25–0.5°/hr drift are used and alignment performed on the ground prior to take-off.

E.3 All-Accelerometer IMUs

Accelerometers are smaller, cheaper, and consume less power than gyros. Consequently, there is interest in using them to sense angular rate. If six accelerometers are arranged such that there are two spatially separated sensors measuring specific force along each axis, angular acceleration may be determined from the difference in the accelerometer outputs (and specific force from the average). However, measuring angular acceleration, as opposed to angular rate, always leads to larger error growth because the attitude errors due to the sensor biases vary quadratically with time instead of linearly.

However, if 12 (or more) accelerometers are used, the angular rate may be deduced from the centrifugal acceleration sensed as the accelerometers rotate about the IMU reference point [11, 12]. Suppose a triad of accelerometers is displaced by a distance \mathbf{r}_{ba}^b from the IMU reference point. If the size effect within the accelerometer triad is neglected then, from (4.11), the specific force sensed by the accelerometers may be expressed in terms of the specific force at the reference point using

$$\mathbf{f}_{ia}^b = \mathbf{f}_{ib}^b + \begin{bmatrix} -(\omega_{ib,y}^b{}^2 + \omega_{ib,z}^b{}^2) & (\omega_{ib,x}^b \omega_{ib,y}^b - \ddot{\omega}_{ib,z}^b) & (\omega_{ib,x}^b \omega_{ib,z}^b + \ddot{\omega}_{ib,y}^b) \\ (\omega_{ib,x}^b \omega_{ib,y}^b + \ddot{\omega}_{ib,z}^b) & -(\omega_{ib,z}^b{}^2 + \omega_{ib,x}^b{}^2) & (\omega_{ib,y}^b \omega_{ib,z}^b - \ddot{\omega}_{ib,x}^b) \\ (\omega_{ib,x}^b \omega_{ib,z}^b - \ddot{\omega}_{ib,y}^b) & (\omega_{ib,y}^b \omega_{ib,z}^b + \ddot{\omega}_{ib,x}^b) & -(\omega_{ib,x}^b{}^2 + \omega_{ib,y}^b{}^2) \end{bmatrix} \mathbf{r}_{ba}^b. \quad (\text{E.3})$$

Rearranging in terms of a measurement matrix, \mathbf{H}_a , and state vector, \mathbf{x} ,

$$\mathbf{f}_{ia}^b = \mathbf{H}_a \mathbf{x}, \quad (\text{E.4})$$

where

$$\mathbf{x} = \begin{pmatrix} f_{ib,x}^b \\ f_{ib,y}^b \\ f_{ib,z}^b \\ \omega_{ib,x}^b{}^2 \\ \omega_{ib,y}^b{}^2 \\ \omega_{ib,z}^b{}^2 \\ \omega_{ib,x}^b \omega_{ib,y}^b \\ \omega_{ib,x}^b \omega_{ib,z}^b \\ \omega_{ib,y}^b \omega_{ib,z}^b \\ \ddot{\omega}_{ib,x}^b \\ \ddot{\omega}_{ib,y}^b \\ \ddot{\omega}_{ib,z}^b \end{pmatrix}. \quad (\text{E.5})$$

and

$$\mathbf{H}_a = \begin{pmatrix} 1 & 0 & 0 & 0 & -x_{ba}^b & -x_{ba}^b & y_{ba}^b & z_{ba}^b & 0 & 0 & z_{ba}^b & -y_{ba}^b \\ 0 & 1 & 0 & -y_{ba}^b & 0 & -y_{ba}^b & x_{ba}^b & 0 & z_{ba}^b & -z_{ba}^b & 0 & x_{ba}^b \\ 0 & 0 & 1 & -z_{ba}^b & -z_{ba}^b & 0 & 0 & x_{ba}^b & y_{ba}^b & y_{ba}^b & -x_{ba}^b & 0 \end{pmatrix} \quad (\text{E.6})$$

With measurements from four accelerometer triads, the state vector can be determined using

$$\mathbf{x} = \begin{pmatrix} \mathbf{H}_1 \\ \mathbf{H}_2 \\ \mathbf{H}_3 \\ \mathbf{H}_4 \end{pmatrix}^{-1} \begin{pmatrix} \mathbf{f}_{i1}^b \\ \mathbf{f}_{i2}^b \\ \mathbf{f}_{i3}^b \\ \mathbf{f}_{i4}^b \end{pmatrix}. \quad (\text{E.7})$$

More generally where measurements from $m \geq 4$ triads are available, the state vector may be determined using least-squares estimation (see Section D.1 of Appendix D on CD). Thus,

$$\mathbf{x} = (\mathbf{H}^T \mathbf{H})^{-1} \mathbf{H}^T \begin{pmatrix} \mathbf{f}_{i1}^b \\ \mathbf{f}_{i2}^b \\ \vdots \\ \mathbf{f}_{im}^b \end{pmatrix}, \quad \mathbf{H} = \begin{pmatrix} \mathbf{H}_1 \\ \mathbf{H}_2 \\ \vdots \\ \mathbf{H}_m \end{pmatrix}. \quad (\text{E.8})$$

The angular rate may then be obtained by taking the square roots of the ω^2 terms. However, there is a sign ambiguity. The ω product terms in \mathbf{x} can be used to reduce the number of possibilities for the ω_{ib}^b vector from eight to two with the remaining ambiguity resolved using the angular acceleration terms and the previous angular rate.

The performance is similar to that obtained with gyros of an equivalent grade [11].

E.4 History of Inertial Navigation

Experimental INS were first developed in the 1920s. However, the sensor and computation technology of the time was not good enough for practical application. The first application of inertial navigation technology was in German V2 rockets during World War II. A partial INS, comprising 3 gyros and a single platform-mounted accelerometer, was used during the initial boost phase only to determine when the desired velocity had been reached and therefore the rocket motor should be shut down; it was not used for the full flight [13].

The first true INSs, capable of useful navigation for an hour or more, were developed in the 1950s. They were initially very large, expensive, and restricted to military use. However, during the 1960s, they were adopted by civil aviation for long-range navigation. In 1968, the Boeing 747 became the first airliner to be fitted with INS as standard and not equipped for astronomical navigation. Shorter range commercial aircraft did not use INS until the 1980s [13].

Early INS were all of the platform configuration, described in Section E.5. They used analog computation and, instead of applying temperature-dependent sensor calibration, were maintained at a stable temperature; this required a 30 minute warm-up period between power-up and alignment.

Strapdown INS were initially deployed in guided weapons where compactness was important and accurate angular rate measurements were needed for the guidance and control system. They replaced platform systems in new aircraft during the 1980s.

E.5 Platform INS

In a strapdown INS, the inertial sensors are fixed with respect to the vehicle body. By contrast, in a *platform INS*, the accelerometer sensitive axes are kept aligned with the north, east, and down axes of a local navigation frame or the axes of a wander azimuth frame. For space

applications, they may be aligned with ECI-frame axes. This is achieved by mounting the accelerometers on a platform which is connected to the INS casing by 3 or 4 rotatable frames, known as *gimbals*. This is shown in Figure E.4. The gyros may be mounted on the platform or at the gimbal axes.

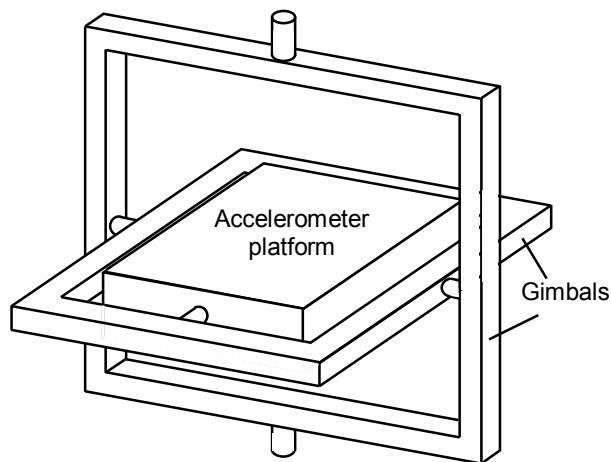


Figure E.4 Gimbaled platform INS

A platform configuration significantly reduces the amount of navigation equations processing that is required. As the accelerometer body frame is kept aligned with the coordinate frame used to resolve the navigation solution, the raw specific-force measurements are already resolved along the axes of that frame. Therefore, the velocity and position may be updated without the need to update the attitude or transform the specific force. A platform inertial navigation processor does not need to input the gyro measurements at all.

The gyros are used to control the gimbal rotation to keep the platform aligned with the reference frame as the host vehicle maneuvers. Traditionally, this was a purely analog process. Further gimbal rotation is instigated to account for the Earth rotation and transport rate (see Section 5.4.1). At initialization, the platform must be physically rotated to align it with the resolving-frame axes.

The main advantage of the platform INS configuration is the much reduced processor load. Hence, all early INS were platform systems and analog computation was initially used. The platform configuration also minimizes the effect of instrument errors excited by host vehicle maneuvers.

Disadvantages of the platform configuration are greater mechanical complexity, size, mass, cost, and power consumption. Furthermore, many platform INS do not output angular rate, while the attitude of the INS body with respect to the resolving frame has traditionally been obtained by directly measuring the gimbal orientations, which has limited accuracy.

Strapdown INS are smaller, mechanically simpler, and thus cheaper than their platform equivalents, while processing capacity is now readily available. The body-resolved inertial sensor measurements can also be used for vehicle control systems, such as autopilots. Consequently, although legacy platform INS are still used in some aircraft, ships, and submarines, new INS are all strapdown systems, except for very high precision systems using PIGA accelerometers. Platform INS are discussed in more detail in [14–17].

E.6 Quaternion Navigation Equations Implementation

This section describes how the inertial navigation equations presented in Chapter 5 may be modified to use the quaternion attitude representation instead of coordinate transformation matrices. This is commonly done to improve processing efficiency.

Section E.6.1 describes quaternion algebra. Section E.6.2 describes the use of quaternions to represent attitude, rotation, and resolving axis transformation. Section E.6.3 then describes the quaternion implementation of the attitude update step of inertial navigation equations. Use

of quaternions for the specific force frame transformation step is not recommended. Note that Section 2.2.3 presents the equations for transforming quaternion attitudes to and from Euler angles and coordinate transformation matrices and Section 2.2.4 presents the equations for transforming between quaternion and rotation vector attitude.

E.6.1 Quaternion Algebra

A quaternion is a hyper-complex number, comprising four components, which may be written as a vector [18]:

$$\mathbf{q} = \begin{pmatrix} q_0 \\ q_1 \\ q_2 \\ q_3 \end{pmatrix}. \quad (\text{E.9})$$

The first component, q_0 , represents the real part of the quaternion, whilst the remaining components are the coefficients of three basis quaternions, \mathbf{i} , \mathbf{j} , and \mathbf{k} , which represent different types of imaginary number. Thus, a generic quaternion is expressed in terms of the basis quaternions using

$$\mathbf{q} = q_0 + q_1\mathbf{i} + q_2\mathbf{j} + q_3\mathbf{k} \quad (\text{E.10})$$

The bases are defined by their behavior under the quaternion product operation, denoted by \circ . Thus [19]:

$$\begin{aligned} \mathbf{i} \circ \mathbf{i} &= -1 & \mathbf{i} \circ \mathbf{j} &= \mathbf{k} & \mathbf{i} \circ \mathbf{k} &= -\mathbf{j} \\ \mathbf{j} \circ \mathbf{i} &= -\mathbf{k} & \mathbf{j} \circ \mathbf{j} &= -1 & \mathbf{j} \circ \mathbf{k} &= \mathbf{i} \\ \mathbf{k} \circ \mathbf{i} &= \mathbf{j} & \mathbf{k} \circ \mathbf{j} &= -\mathbf{i} & \mathbf{k} \circ \mathbf{k} &= -1 \end{aligned} \quad (\text{E.11})$$

The quaternion bases may also be expressed as 4×4 matrices [20].

Quaternions are added and subtracted simply by adding and subtracting the constituent components. Thus:

$$\mathbf{p} + \mathbf{q} = \begin{pmatrix} p_0 \\ p_1 \\ p_2 \\ p_3 \end{pmatrix} + \begin{pmatrix} q_0 \\ q_1 \\ q_2 \\ q_3 \end{pmatrix} = \begin{pmatrix} p_0 + q_0 \\ p_1 + q_1 \\ p_2 + q_2 \\ p_3 + q_3 \end{pmatrix}. \quad (\text{E.12})$$

A quaternion product is determined as follows:

$$\begin{aligned} \mathbf{p} \circ \mathbf{q} &= (p_0 + p_1\mathbf{i} + p_2\mathbf{j} + p_3\mathbf{k}) \circ (q_0 + q_1\mathbf{i} + q_2\mathbf{j} + q_3\mathbf{k}) \\ &= p_0q_0 + p_0q_1\mathbf{i} + p_0q_2\mathbf{j} + p_0q_3\mathbf{k} + p_1q_0\mathbf{i} + p_1q_1\mathbf{i} \circ \mathbf{i} + p_1q_2\mathbf{i} \circ \mathbf{j} + p_1q_3\mathbf{i} \circ \mathbf{k} \\ &\quad + p_2q_0\mathbf{j} + p_2q_1\mathbf{j} \circ \mathbf{i} + p_2q_2\mathbf{j} \circ \mathbf{j} + p_2q_3\mathbf{j} \circ \mathbf{k} + p_3q_0\mathbf{k} + p_3q_1\mathbf{k} \circ \mathbf{i} + p_3q_2\mathbf{k} \circ \mathbf{j} + p_3q_3\mathbf{k} \circ \mathbf{k} \end{aligned} \quad (\text{E.13})$$

Applying (E.11),

$$\begin{aligned} \mathbf{p} \circ \mathbf{q} &= p_0q_0 + p_0q_1\mathbf{i} + p_0q_2\mathbf{j} + p_0q_3\mathbf{k} + p_1q_0\mathbf{i} + p_1q_1\mathbf{i} \circ \mathbf{i} + p_1q_2\mathbf{i} \circ \mathbf{j} + p_1q_3\mathbf{i} \circ \mathbf{k} \\ &\quad + p_2q_0\mathbf{j} + p_2q_1\mathbf{j} \circ \mathbf{i} + p_2q_2\mathbf{j} \circ \mathbf{j} + p_2q_3\mathbf{j} \circ \mathbf{k} + p_3q_0\mathbf{k} + p_3q_1\mathbf{k} \circ \mathbf{i} + p_3q_2\mathbf{k} \circ \mathbf{j} + p_3q_3\mathbf{k} \circ \mathbf{k} \\ &= (p_0q_0 - p_1q_1 - p_2q_2 - p_3q_3) + (p_0q_1 + p_1q_0 + p_2q_3 - p_3q_2)\mathbf{i} \\ &\quad + (p_0q_2 - p_1q_3 + p_2q_0 + p_3q_1)\mathbf{j} + (p_0q_3 + p_1q_2 - p_2q_1 + p_3q_0)\mathbf{k} \end{aligned} \quad (\text{E.14})$$

In vector form,

$$\begin{aligned} \mathbf{p} \circ \mathbf{q} &= \begin{pmatrix} p_0 q_0 - p_1 q_1 - p_2 q_2 - p_3 q_3 \\ p_0 q_1 + p_1 q_0 + p_2 q_3 - p_3 q_2 \\ p_0 q_2 - p_1 q_3 + p_2 q_0 + p_3 q_1 \\ p_0 q_3 + p_1 q_2 - p_2 q_1 + p_3 q_0 \end{pmatrix} \\ &= \begin{pmatrix} p_0 & -p_1 & -p_2 & -p_3 \\ p_1 & p_0 & -p_3 & p_2 \\ p_2 & p_3 & p_0 & -p_1 \\ p_3 & -p_2 & p_1 & p_0 \end{pmatrix} \begin{pmatrix} q_0 \\ q_1 \\ q_2 \\ q_3 \end{pmatrix} = \begin{pmatrix} q_0 & -q_1 & -q_2 & -q_3 \\ q_1 & q_0 & q_3 & -q_2 \\ q_2 & -q_3 & q_0 & q_1 \\ q_3 & q_2 & -q_1 & q_0 \end{pmatrix} \begin{pmatrix} p_0 \\ p_1 \\ p_2 \\ p_3 \end{pmatrix}. \end{aligned} \quad (\text{E.15})$$

Like matrices, quaternions do not commute, so reversing the order of multiplication changes the result:

$$\mathbf{p} \circ \mathbf{q} \neq \mathbf{q} \circ \mathbf{p}. \quad (\text{E.16})$$

However, quaternions are associative. Thus:

$$\begin{aligned} (\mathbf{p} \circ \mathbf{q}) \circ \mathbf{r} &= \mathbf{p} \circ (\mathbf{q} \circ \mathbf{r}) \\ (\mathbf{p} + \mathbf{q}) \circ \mathbf{r} &= (\mathbf{p} \circ \mathbf{r}) + (\mathbf{q} \circ \mathbf{r}). \end{aligned} \quad (\text{E.17})$$

A quaternion and a 3-component vector may be multiplied by treating the vector as a quaternion with the real component set to zero. Thus

$$\mathbf{a} \circ \mathbf{q} = \begin{pmatrix} -a_1 q_1 - a_2 q_2 - a_3 q_3 \\ +a_1 q_0 + a_2 q_3 - a_3 q_2 \\ -a_1 q_3 + a_2 q_0 + a_3 q_1 \\ +a_1 q_2 - a_2 q_1 + a_3 q_0 \end{pmatrix} \quad \mathbf{q} \circ \mathbf{a} = \begin{pmatrix} -q_1 a_1 - q_2 a_2 - q_3 a_3 \\ q_0 a_1 + q_2 a_3 - q_3 a_2 \\ q_0 a_2 - q_1 a_3 + q_3 a_1 \\ q_0 a_3 + q_1 a_2 - q_2 a_1 \end{pmatrix}. \quad (\text{E.18})$$

The conjugate of a quaternion is analogous to that of a complex number; the sign of the three imaginary components is reversed. Thus,

$$\mathbf{q}^* = \begin{pmatrix} q_0 \\ -q_1 \\ -q_2 \\ -q_3 \end{pmatrix}. \quad (\text{E.19})$$

The product of a quaternion with its conjugate is always real. This is used to generate the norm:

$$|\mathbf{q}| = \sqrt{\mathbf{q} \circ \mathbf{q}^*} = \sqrt{q_0^2 + q_1^2 + q_2^2 + q_3^2}. \quad (\text{E.20})$$

The inverse of a quaternion is given by

$$\mathbf{q}^{-1} = \frac{\mathbf{q}^*}{|\mathbf{q}|^2} = \frac{\mathbf{q}^*}{\mathbf{q} \circ \mathbf{q}^*}. \quad (\text{E.21})$$

A unit quaternion has the properties

$$|\mathbf{q}| = 1 \quad \mathbf{q}^{-1} = \mathbf{q}^*. \quad (\text{E.22})$$

E.6.2 Attitude, Rotation, and Resolving Axes Transformations

The quaternion representing the attitude of frame α with respect to frame β or the rotation from frame β to frame α is

$$\mathbf{q}_{\beta}^{\alpha} = \begin{pmatrix} \cos(\mu_{\beta\alpha}/2) \\ e_{\beta\alpha,1}^{\alpha/\beta} \sin(\mu_{\beta\alpha}/2) \\ e_{\beta\alpha,2}^{\alpha/\beta} \sin(\mu_{\beta\alpha}/2) \\ e_{\beta\alpha,3}^{\alpha/\beta} \sin(\mu_{\beta\alpha}/2) \end{pmatrix}, \quad (\text{E.23})$$

where $\mu_{\beta\alpha}$ is the magnitude of the rotation and $\mathbf{e}_{\beta\alpha}^{\alpha/\beta}$ is the axis-of-rotation unit vector; both are defined in Section 2.2.2.

To reverse a rotation, the conjugate of the quaternion is used. Thus,

$$\mathbf{q}_{\alpha}^{\beta} = \mathbf{q}_{\beta}^{\alpha *} . \quad (\text{E.24})$$

This is equivalent to reversing the sign of either $\mu_{\beta\alpha}$ or $\mathbf{e}_{\beta\alpha}^{\alpha/\beta}$, either of which will reverse the direction of rotation.

To perform successive rotations, the quaternions are simply multiplied:

$$\mathbf{q}_{\alpha}^{\gamma} = \mathbf{q}_{\alpha}^{\beta} \circ \mathbf{q}_{\beta}^{\gamma}, \quad (\text{E.25})$$

noting that the order is critical as rotations themselves do not commute (see Figure 2.10) and is the opposite of that for coordinate transformation matrices. Thus,

$$\mathbf{q}_{\alpha}^{\gamma} \neq \mathbf{q}_{\beta}^{\gamma} \circ \mathbf{q}_{\alpha}^{\beta}. \quad (\text{E.26})$$

Combining two rotations using quaternions requires the computation of 16 scalar multiplications, whereas the equivalent process using coordinate transformation matrices requires 27 multiplications, a factor of 1.69 more. Consequently, a quaternion-based attitude update algorithm is more computationally efficient than its coordinate transformation matrix equivalent.

By analogy with its coordinate transformation matrix counterpart (see Section 5.7), the quaternion form of the attitude error is defined as

$$\delta \mathbf{q}_{\beta}^{\alpha} = \mathbf{q}_{\alpha}^{\beta} \circ \tilde{\mathbf{q}}_{\beta}^{\alpha}, \quad (\text{E.27})$$

where ‘ \sim ’ denotes the computed attitude and its absence denotes the true attitude.

From (E.23), a quaternion representing a zero rotation is simply 1. Thus,

$$\begin{aligned} \mathbf{q}_{\alpha}^{\alpha} &= \mathbf{q}_{\alpha}^{\beta} \circ \mathbf{q}_{\beta}^{\alpha} = 1 \\ \Rightarrow \mathbf{q}_{\beta}^{\alpha} &= \mathbf{q}_{\alpha}^{\alpha} \circ \mathbf{q}_{\beta}^{\alpha} = 1 \end{aligned} \quad (\text{E.28})$$

The attitude quaternion is therefore a unit quaternion. This removes one degree of freedom, so only three of the four components of an attitude quaternion are independent (noting that the axis-of-rotation unit vector only has two independent components).

To perform a resolving-axes transformation using quaternion attitude, two quaternion multiplications are required:

$$\mathbf{x}^{\beta} = \mathbf{q}_{\beta}^{\alpha} \circ \mathbf{x}^{\alpha} \circ \mathbf{q}_{\alpha}^{\beta}. \quad (\text{E.29})$$

This requires 32 scalar multiplications, as opposed to 9 using a coordinate transformation matrix. Quaternion texts (e.g., [18]) recommend a method that is equivalent to calculating the corresponding coordinate transformation matrix from the quaternion and then using that to transform the resolving axes of the vector; this requires 19 scalar multiplications altogether.

Consider a quaternion representing a small angle rotation. This may be expressed as

$$\delta \mathbf{q}_\beta^\alpha = \begin{pmatrix} 1 \\ e^{\alpha/\beta} \delta \mu_{\beta\alpha,1}/2 \\ e^{\alpha/\beta} \delta \mu_{\beta\alpha,2}/2 \\ e^{\alpha/\beta} \delta \mu_{\beta\alpha,3}/2 \end{pmatrix}. \quad (\text{E.30})$$

Applying this in (E.25) and differentiating the rotation with respect to time, the time derivative of quaternion attitude may be obtained [18]:

$$\dot{\mathbf{q}}_\beta^\alpha = \mathbf{q}_\beta^\alpha \circ \begin{pmatrix} 0 \\ \omega_{\beta\alpha,x}^\alpha/2 \\ \omega_{\beta\alpha,y}^\alpha/2 \\ \omega_{\beta\alpha,z}^\alpha/2 \end{pmatrix} = \frac{1}{2} \mathbf{q}_\beta^\alpha \circ \begin{pmatrix} 0 \\ \boldsymbol{\omega}_{\beta\alpha}^\alpha \end{pmatrix} = \begin{pmatrix} 0 \\ \omega_{\beta\alpha,x}^\beta/2 \\ \omega_{\beta\alpha,y}^\beta/2 \\ \omega_{\beta\alpha,z}^\beta/2 \end{pmatrix} \circ \mathbf{q}_\beta^\alpha = \frac{1}{2} \begin{pmatrix} 0 \\ \boldsymbol{\omega}_{\beta\alpha}^\beta \end{pmatrix} \circ \mathbf{q}_\beta^\alpha, \quad (\text{E.31})$$

where $\boldsymbol{\omega}_{\beta\alpha}^\gamma$ is the angular rate of frame a with respect to frame b, resolved about the axes of frame γ . Applying (E.15), this may be expressed using matrix multiplication as

$$\dot{\mathbf{q}}_\beta^\alpha = \frac{1}{2} \begin{pmatrix} 0 & -\omega_{\beta\alpha,x}^\alpha & -\omega_{\beta\alpha,y}^\alpha & -\omega_{\beta\alpha,z}^\alpha \\ \omega_{\beta\alpha,x}^\alpha & 0 & \omega_{\beta\alpha,z}^\alpha & -\omega_{\beta\alpha,y}^\alpha \\ \omega_{\beta\alpha,y}^\alpha & -\omega_{\beta\alpha,z}^\alpha & 0 & \omega_{\beta\alpha,x}^\alpha \\ \omega_{\beta\alpha,z}^\alpha & \omega_{\beta\alpha,y}^\alpha & -\omega_{\beta\alpha,x}^\alpha & 0 \end{pmatrix} \mathbf{q}_\beta^\alpha = \frac{1}{2} \begin{pmatrix} 0 & -\omega_{\beta\alpha,x}^\beta & -\omega_{\beta\alpha,y}^\beta & -\omega_{\beta\alpha,z}^\beta \\ \omega_{\beta\alpha,x}^\beta & 0 & -\omega_{\beta\alpha,z}^\beta & \omega_{\beta\alpha,y}^\beta \\ \omega_{\beta\alpha,y}^\beta & \omega_{\beta\alpha,z}^\beta & 0 & -\omega_{\beta\alpha,x}^\beta \\ \omega_{\beta\alpha,z}^\beta & -\omega_{\beta\alpha,y}^\beta & \omega_{\beta\alpha,x}^\beta & 0 \end{pmatrix} \mathbf{q}_\beta^\alpha. \quad (\text{E.32})$$

E.6.3 Attitude Update

From (E.31), the time derivative of the quaternion attitude solution may be expressed as

$$\dot{\mathbf{q}}_\gamma^b = \frac{1}{2} \mathbf{q}_\gamma^b \circ \begin{pmatrix} 0 \\ \boldsymbol{\omega}_{\gamma b}^b \end{pmatrix} = \frac{1}{2} \begin{pmatrix} 0 \\ \boldsymbol{\omega}_{\gamma b}^\gamma \end{pmatrix} \circ \mathbf{q}_\gamma^b \quad \gamma \in i, e, n, \quad (\text{E.33})$$

Making the same assumptions as for the coordinate transformation matrix equivalents presented in Sections 5.2.1, 5.3.1, and 5.4.1, the quaternion attitude update equations to first-order in $\boldsymbol{\omega}_{ib}^b \tau_i$ are

$$\mathbf{q}_i^b(+) \approx \mathbf{q}_i^b(-) \circ \begin{pmatrix} 1 \\ \frac{1}{2} \boldsymbol{\omega}_{ib}^b \tau_i \end{pmatrix} \quad (\text{E.34})$$

for the ECI-frame implementation,

$$\mathbf{q}_e^b(+) \approx \mathbf{q}_e^b(-) \circ \begin{pmatrix} 1 \\ \frac{1}{2} \boldsymbol{\omega}_{ib}^b \tau_i \end{pmatrix} - \begin{pmatrix} 0 \\ \frac{1}{2} \boldsymbol{\omega}_{ie}^e \tau_i \end{pmatrix} \circ \mathbf{q}_e^b(-) \quad (\text{E.35})$$

for the ECEF-frame implementation, and

$$\mathbf{q}_n^b(+) \approx \mathbf{q}_n^b(-) \circ \begin{pmatrix} 1 \\ \frac{1}{2} \boldsymbol{\omega}_{ib}^b \tau_i \end{pmatrix} - \begin{pmatrix} 0 \\ \frac{1}{2} (\boldsymbol{\omega}_{ie}^n + \boldsymbol{\omega}_{en}^n) \tau_i \end{pmatrix} \circ \mathbf{q}_n^b(-) \quad (\text{E.36})$$

for the local-navigation-frame implementation, where the suffixes $(-)$ and $(+)$ denote before and after the update, respectively. Where the IMU outputs attitude increments, $\boldsymbol{\alpha}_{ib}^b$, these can be used in place of $\boldsymbol{\omega}_{ib}^b \tau_i$.

The precision ECI-frame attitude update may be formulated as

$$\mathbf{q}_i^b(+) = \mathbf{q}_i^b(-) \circ \mathbf{q}_{b-}^{b+}, \quad (\text{E.37})$$

where \mathbf{q}_{b-}^{b+} is the attitude update quaternion, given by

$$\mathbf{q}_{b-}^{b+} = \begin{pmatrix} \cos(|\boldsymbol{\alpha}_{ib}^b|/2) \\ \frac{\sin(|\boldsymbol{\alpha}_{ib}^b|/2)}{|\boldsymbol{\alpha}_{ib}^b|} \boldsymbol{\alpha}_{ib}^b \end{pmatrix}. \quad (\text{E.38})$$

Where successive IMU outputs are combined, \mathbf{p}_{b-b+} (see Section 5.5.4) may be used in place of $\boldsymbol{\alpha}_{ib}^b$. Approximations of the form

$$\mathbf{q}_{b-}^{b+} \approx \begin{pmatrix} a_c \\ a_s \boldsymbol{\alpha}_{ib}^b \end{pmatrix} \quad (\text{E.39})$$

may also be used, where Table E.1 gives the coefficients and drift rate for algorithms using the first- to fourth-order approximations [8]. Comparing this with Table 5.1, it can be seen that a first- or second-order quaternion algorithm produces the same drift as the corresponding coordinate transformation matrix algorithm with half the attitude increment. Thus, in principle, a quaternion attitude update can achieve the same precision as an equivalent coordinate transformation matrix algorithm running at twice the iteration rate. This is because the coordinate transformation matrix implementation of the attitude update is based on a power-series expansion of a function of $\boldsymbol{\alpha}_{ib}^b$, whereas the quaternion implementation is based on the expansion of functions of $\boldsymbol{\alpha}_{ib}^b / 2$.

The precision ECEF-frame and local-navigation-frame attitude update equations are similarly

$$\mathbf{q}_e^b(+) = \mathbf{q}_e^b(-) \circ \mathbf{q}_{b-}^{b+} - \begin{pmatrix} 0 \\ \frac{1}{2} \boldsymbol{\omega}_{ie}^e \boldsymbol{\tau}_i \end{pmatrix} \circ \mathbf{q}_e^b(-), \quad (\text{E.40})$$

$$\mathbf{q}_n^b(+) \approx \mathbf{q}_n^b(-) \circ \mathbf{q}_{b-}^{b+} - \begin{pmatrix} 0 \\ \frac{1}{2} (\boldsymbol{\omega}_{ie}^n(-) + \boldsymbol{\omega}_{en}^n(-)) \boldsymbol{\tau}_i \end{pmatrix} \circ \mathbf{q}_n^b(-). \quad (\text{E.41})$$

Table E.1 Coefficients and Drift of Attitude Update Algorithms Using First- to Fourth-order Approximations

Algorithm Order	Coefficient a_c	Attitude Drift at 100-Hz update rate, rad s^{-1} ($^\circ \text{hr}^{-1}$)		
		Coefficient a_s	$ \boldsymbol{\alpha} = 0.1 \text{ rad step size}$	$ \boldsymbol{\alpha} = 0.05 \text{ rad step size}$
1	1	0.5	8.3×10^{-3} (1720)	2.1×10^{-3} (430)
2	$1 - \frac{1}{2} \left(\frac{ \boldsymbol{\alpha}_{ib}^b }{2} \right)^2$	0.5	4.2×10^{-3} (860)	1.1×10^{-3} (215)
3	$1 - \frac{1}{2} \left(\frac{ \boldsymbol{\alpha}_{ib}^b }{2} \right)^2$	$\frac{1}{2} - \frac{1}{12} \left(\frac{ \boldsymbol{\alpha}_{ib}^b }{2} \right)^2$	2.5×10^{-6} (0.4)	2.9×10^{-7} (0.06)
4	$1 - \frac{1}{2} \left(\frac{ \boldsymbol{\alpha}_{ib}^b }{2} \right)^2 + \frac{1}{24} \left(\frac{ \boldsymbol{\alpha}_{ib}^b }{2} \right)^4$	$\frac{1}{2} - \frac{1}{12} \left(\frac{ \boldsymbol{\alpha}_{ib}^b }{2} \right)^2$	1.3×10^{-6} (0.2)	2.9×10^{-7} (0.06)

The precision high-dynamics local-navigation-frame attitude update equations is

$$\mathbf{q}_n^b(+) \approx \mathbf{q}_n^b(-) \circ \mathbf{q}_{b-}^{b+} - \left(\begin{pmatrix} 0 \\ \frac{1}{2} \boldsymbol{\omega}_{ie}^n(-) + \frac{1}{4} \boldsymbol{\omega}_{en}^n(-) + \frac{1}{4} \boldsymbol{\omega}_{en}^n(-) \end{pmatrix} \tau_i \right) \circ \mathbf{q}_n^b(-). \quad (\text{E.42})$$

To maintain the attitude as a unit quaternion where approximations are used and computational rounding errors are present, it must be periodically normalized using.

$$\mathbf{q}_\gamma^b(+) = \frac{\mathbf{q}_\gamma^b(-)}{\sqrt{\mathbf{q}_\gamma^b(-) \circ \mathbf{q}_\gamma^b(-)^*}} \quad \gamma \in i, e, n. \quad (\text{E.43})$$

The quaternion attitude solution may be corrected using a small-angle attitude error estimate from a Kalman filter using

$$\hat{\mathbf{q}}_\gamma^b = \left(\begin{pmatrix} 1 \\ -\frac{1}{2} \delta \hat{\boldsymbol{\psi}}_{\gamma b}^\gamma \end{pmatrix} \right) \circ \tilde{\mathbf{q}}_\gamma^b, \quad (\text{E.44})$$

for open-loop integration (see Section 14.1.1), where $\delta \hat{\boldsymbol{\psi}}_{\gamma b}^\gamma$ is the Kalman filter estimate of the attitude error of the INS body frame, b , with respect to frame γ , resolved about the frame γ axes, ‘ \wedge ’ denotes the corrected attitude solution, and ‘ \sim ’ denotes the raw attitude solution.

For closed-loop integration (see Section 14.1.1), new corrections are applied using

$$\hat{\mathbf{q}}_\gamma^b(+) = \left(\begin{pmatrix} 1 \\ -\frac{1}{2} \delta \hat{\boldsymbol{\psi}}_{\gamma b}^\gamma \end{pmatrix} \right) \circ \hat{\mathbf{q}}_\gamma^b(-). \quad (\text{E.45})$$

E.7 Local Tangent-Plane Frame Navigation Equations

A local tangent-plane frame, defined in Section 2.1.4, is used for navigation within a localized area. This frame is Earth fixed, so the navigation equations have a similar form to the ECEF-frame equations, described in Sections 5.3 and 5.5. Therefore, the derivation is not presented. The resolving axes and reference frame of a navigation solution may be converted between the ECEF and local-tangent-plane frames by performing a rotation and translation as described in Section 2.5.4.

The first-order attitude update is

$$\mathbf{C}_b^l(+) \approx \mathbf{C}_b^l(-) \left(\mathbf{I}_3 + \boldsymbol{\Omega}_{ib}^b \tau_i \right) - \boldsymbol{\Omega}_{il}^l \mathbf{C}_b^l(-) \tau_i. \quad (\text{E.46})$$

where the skew-symmetric matrix of the angular rate of the local tangent-plane frame with respect to the ECI frame is

$$\boldsymbol{\Omega}_{il}^l = \mathbf{C}_e^l \boldsymbol{\Omega}_{ie}^e \mathbf{C}_l^e \quad (\text{E.47})$$

and the other terms are as defined in Chapter 5. Note that \mathbf{C}_e^l is constant because both frames are Earth fixed. The precise attitude update is

$$\mathbf{C}_b^l(+) \approx \mathbf{C}_b^l(-) \mathbf{C}_{b+}^{b-} - \boldsymbol{\Omega}_{il}^l \mathbf{C}_b^l(-) \tau_i, \quad (\text{E.48})$$

where the attitude update matrix, \mathbf{C}_{b+}^{b-} , is given by (5.73).

The approximate specific-force frame transformation is

$$\begin{aligned} \mathbf{f}_{ib}^l &\approx \frac{1}{2} \left(\mathbf{C}_b^l(-) + \mathbf{C}_b^l(+) \right) \mathbf{f}_{ib}^b \\ \mathbf{v}_{ib}^l &\approx \frac{1}{2} \left(\mathbf{C}_b^l(-) + \mathbf{C}_b^l(+) \right) \mathbf{v}_{ib}^b \end{aligned} \quad (\text{E.49})$$

while the precise transformation is

$$\mathbf{f}_{ib}^l = \overline{\mathbf{C}}_b^l \mathbf{f}_{ib}^b, \quad \overline{\mathbf{C}}_b^l = \mathbf{C}_b^l(-) \mathbf{C}_b^{b-} - \frac{1}{2} \boldsymbol{\Omega}_{il}^l \mathbf{C}_b^l(-) \tau_i \quad (\text{E.50})$$

where $\mathbf{C}_{\bar{b}}^{b-}$ is given by (5.84).

Neglecting the variation of the Coriolis term over the update interval, the velocity may be updated using

$$\begin{aligned}\mathbf{v}_{lb}^l(+) &\approx \mathbf{v}_{lb}^l(-) + \left(\mathbf{f}_{ib}^l + \mathbf{C}_e^l \mathbf{g}_b^e(\mathbf{r}_{eb}^e(-)) - 2\boldsymbol{\Omega}_{il}^l \mathbf{v}_{lb}^l(-) \right) \tau_i, \\ &= \mathbf{v}_{lb}^l(-) + \mathbf{v}_{ib}^l + \left(\mathbf{C}_e^l \mathbf{g}_b^e(\mathbf{r}_{eb}^e(-)) - 2\boldsymbol{\Omega}_{il}^l \mathbf{v}_{lb}^l(-) \right) \tau_i,\end{aligned}\quad (\text{E.51})$$

where \mathbf{r}_{eb}^e is obtained from \mathbf{r}_{lb}^l using (2.160).

Finally, the position is updated using

$$\begin{aligned}\mathbf{r}_{lb}^l(+) &= \mathbf{r}_{lb}^l(-) + \left(\mathbf{v}_{lb}^l(-) + \mathbf{v}_{lb}^l(+) \right) \frac{\tau_i}{2} \\ &\approx \mathbf{r}_{lb}^l(-) + \mathbf{v}_{lb}^l(-) \tau_i + \left(\mathbf{f}_{ib}^l + \mathbf{C}_e^l \mathbf{g}_b^e(\mathbf{r}_{eb}^e(-)) - 2\boldsymbol{\Omega}_{il}^l \mathbf{v}_{lb}^l(-) \right) \frac{\tau_i^2}{2}.\end{aligned}\quad (\text{E.52})$$

E.8 Navigation Equations Iteration Rate Issues

Best efficiency may sometimes be achieved by iterating different stages of the inertial navigations mechanization at different rates. However, it should be noted that there is no benefit in using a smaller step in a stage of inertial navigation processing than was used in the preceding stages. For example, the position increment from time t to time $t + \tau_i$ is obtained by integrating the velocity. Figure E.5 (a) shows that where the velocity is only known at the beginning and end of the integration interval, dividing the integral into two trapezoids does not change the result. Figure E.5 (b) shows that where the velocity is also known at the halfway point, dividing the position integral into two trapezoids does improve precision. However, the velocity from before time t and after time $t + \tau_i$ may be used to help estimate the variation of velocity between times t and $t + \tau_i$.

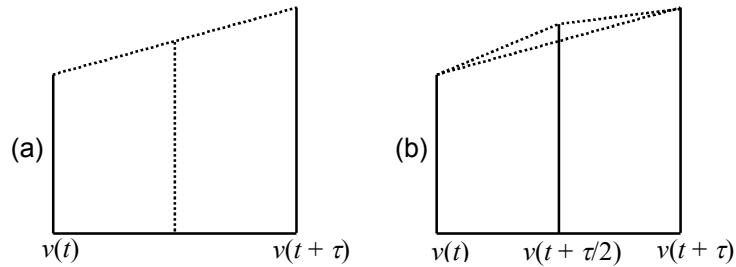


Figure E.5 Integration of velocity to obtain position. (From: [21]. ©2002 QinetiQ Ltd. Reprinted with permission.)

Where a stage of the inertial navigation equations inputs data at a higher iteration rate than it is required to output at, higher-order numerical integration techniques may be used to mechanize the inertial navigation equations. For example, a fourth-order Runge-Kutta algorithm integrates

$$\mathbf{x}(t + \tau) = \mathbf{x}(t) + \int_t^{t+\tau} \mathbf{g}(\mathbf{x}(t), \mathbf{u}(t)) dt \quad (\text{E.53})$$

in five steps:

$$\begin{aligned}
\mathbf{k}_1 &= \mathbf{g}(\mathbf{x}(t), \mathbf{u}(t)) \\
\mathbf{k}_2 &= \mathbf{g}\left(\left(\mathbf{x}(t) + \frac{1}{2}\tau\mathbf{k}_1\right), \mathbf{u}\left(t + \frac{1}{2}\tau\right)\right) \\
\mathbf{k}_3 &= \mathbf{g}\left(\left(\mathbf{x}(t) + \frac{1}{2}\tau\mathbf{k}_2\right), \mathbf{u}\left(t + \frac{1}{2}\tau\right)\right) \\
\mathbf{k}_4 &= \mathbf{g}(\mathbf{x}(t) + \tau\mathbf{k}_3, \mathbf{u}(t + \tau)) \\
\mathbf{x}(t + \tau) &= \mathbf{x}(t) + \frac{1}{6}\tau(\mathbf{k}_1 + 2\mathbf{k}_2 + 2\mathbf{k}_3 + \mathbf{k}_4)
\end{aligned} \tag{E.54}$$

This approach is sometimes used for the position update stage [8]. It may also be applied to the processing cycle as a whole. However, caution should be exercised in passing data from one step to another in blocks of several time epochs. For example, where the local-navigation-frame equations are used (Section 5.4), the attitude and velocity integrations are a function of position. Therefore, stepping through the complete navigation equations cycle at a higher rate will generally be more accurate than passing intermediate outputs from one step to the next.

Where exact navigation equations are used, there is no benefit in processing them at a higher iteration rate than the IMU output rate unless interpolations are required. However, where approximations are made, some stages, such as the attitude update and specific-force frame transformation, can benefit from a higher iteration rate. For example, iterating the first-order attitude update at twice the IMU rate requires a similar processor load to iterating the second-order update at the IMU rate, but is more accurate and simpler to code. However, the fourth-order update is much more accurate and requires only slightly more processing than the second-order update.

E.9 Effects of Timing Errors

The poorest quality clock that might be used with an inertial navigation processor is a basic quartz crystal oscillator, accurate to one part in 10^5 . Better timing accuracy may be achieved using a higher quality clock (see Section 9.1.2) and/or by using an external timing reference, such as GNSS.

Timing errors can affect inertial navigation in four main ways. Firstly, errors in the integration (where required) of the specific force and angular rate measurements to update the velocity and attitude will behave as a scale factor error common to all sensors. However, at no more than 10 ppm, it will be smaller than the scale factor errors of the sensors themselves (with the exception of some RLGs), so can usually be neglected.

Secondly, the error in the integration of the acceleration due to gravity in the velocity update step will give a vertical acceleration error of up to 10^{-4} m s^{-2} ($10 \mu\text{g}$), which is smaller than the bias of most accelerometers.

Thirdly, there will be an error in the integration of the velocity to update the position. This is only significant for space and hypersonic flight applications, for which other error sources will typically dominate.

The final effect is the mistiming of the Earth's rotation. This introduces an east velocity error of up to 5 mm s^{-1} , which is only significant for the highest precision applications.

E.10 Pseudo-measurement Generation using Motion Constraints

The motion constraints of a land vehicle (see Section 5.9) may be used to generate roll- and pitch-axis angular rate pseudo-measurements from the accelerometer and yaw-axis gyro measurements of a partial IMU.

It is convenient to define a rear-wheel body frame, denoted r , that is centered equidistant between the rear wheels along their axis of rotation and aligned with their direction of travel. It is assumed that the axes of the IMU body frame, b , are aligned with the r frame (i.e., $\mathbf{C}_r^b = \mathbf{I}_3$). The motion constraints may thus be expressed as

$$\mathbf{v}_{er}^r = \begin{pmatrix} v_{er,x}^r \\ 0 \\ 0 \end{pmatrix}. \quad (\text{E.55})$$

The ECEF-frame velocity update equation is, [repeating (5.36)],

$$\mathbf{v}_{eb}^e(+) \approx \mathbf{v}_{eb}^e(-) + (\mathbf{f}_{ib}^e + \mathbf{g}_b^e(\mathbf{r}_{eb}^e(-)) - 2\boldsymbol{\Omega}_{ie}^e \mathbf{v}_{eb}^e(-))\tau_i.$$

Applying (2.73), (2.165), and (5.28),

$$\begin{aligned} & \mathbf{C}_b^e(+)(\mathbf{v}_{er}^r(+) + \boldsymbol{\omega}_{eb}^b(+) \wedge \mathbf{l}_{rb}^b) = \\ & \mathbf{C}_b^e(-)(\mathbf{v}_{er}^r(-) + \boldsymbol{\omega}_{eb}^b(-) \wedge \mathbf{l}_{rb}^b) + \frac{1}{2}(\mathbf{C}_b^e(+) + \mathbf{C}_b^e(-))\mathbf{f}_{ib}^b\tau_i + [\mathbf{g}_b^e(\mathbf{r}_{eb}^e(-)) - 2\boldsymbol{\Omega}_{ie}^e \mathbf{v}_{eb}^e(-)]\tau_i, \end{aligned} \quad (\text{E.56})$$

where \mathbf{l}_{rb}^b is the lever arm from the r frame to the b frame. Where a partial IMU is used, it may be assumed that the gyro errors are substantially larger than the Earth rotation rate. Therefore, the Earth-rate terms in (E.56) may be neglected, giving

$$\begin{aligned} & \mathbf{C}_b^e(+)(\mathbf{v}_{er}^r(+) + \boldsymbol{\omega}_{eb}^b(+) \wedge \mathbf{l}_{rb}^b) \approx \\ & \mathbf{C}_b^e(-)(\mathbf{v}_{er}^r(-) + \boldsymbol{\omega}_{eb}^b(-) \wedge \mathbf{l}_{rb}^b) + \frac{1}{2}(\mathbf{C}_b^e(+) + \mathbf{C}_b^e(-))\mathbf{f}_{ib}^b\tau_i + \mathbf{g}_b^e(\mathbf{r}_{eb}^e(-))\tau_i. \end{aligned} \quad (\text{E.57})$$

From (5.68), where the Earth rate is neglected,

$$\mathbf{C}_b^e(+) \approx \mathbf{C}_b^e(-)\mathbf{C}_{b+}^{b-}. \quad (\text{E.58})$$

Substituting (E.58) and (E.55) into (E.57), and canceling $\mathbf{C}_b^e(-)$,

$$\mathbf{C}_{b+}^{b-} \left(\begin{pmatrix} v_{er,x}^r(+) \\ 0 \\ 0 \end{pmatrix} + \boldsymbol{\omega}_{eb}^b(+) \wedge \mathbf{l}_{rb}^b \right) \approx \left(\begin{pmatrix} v_{er,x}^r(-) \\ 0 \\ 0 \end{pmatrix} + \boldsymbol{\omega}_{eb}^b(-) \wedge \mathbf{l}_{rb}^b \right) + \frac{1}{2}(\mathbf{I}_3 + \mathbf{C}_{b+}^{b-})\mathbf{f}_{ib}^b\tau_i + \mathbf{g}_b^b(-)\tau_i, \quad (\text{E.59})$$

where $\mathbf{g}_b^b(-) = \mathbf{C}_e^b(-)\mathbf{g}_b^e(\mathbf{r}_{eb}^e(-))$. Where the small angle approximation is applied to the attitude increment and the angular acceleration about the x - and y -axes is neglected, this simplifies to

$$(\mathbf{I}_3 + \boldsymbol{\Omega}_{ib}^b\tau_i) \begin{pmatrix} v_{er,x}^r(+) \\ 0 \\ 0 \end{pmatrix} \approx \begin{pmatrix} v_{er,x}^r(-) + \mathbf{g}_{b,x}^b(-)\tau_i \\ \mathbf{g}_{b,y}^b(-)\tau_i - \dot{\omega}_{ib,z}^b l_{rb,x}^b\tau_i \\ \mathbf{g}_{b,z}^b(-)\tau_i \end{pmatrix} + \left(\mathbf{I}_3 + \frac{1}{2}\boldsymbol{\Omega}_{ib}^b\tau_i \right) \mathbf{f}_{ib}^b\tau_i. \quad (\text{E.60})$$

Eliminating $v_{er,x}^r(+)$ (which is unknown at this point) and then solving for the x - and y -axis angular acceleration under the assumption that attitude increment products may be neglected under the small angle approximation gives the following pseudo-measurements

$$\begin{aligned} \omega_{ib,x}^b & \approx \frac{1}{f_{ib,z}^b\tau_i} [2(\mathbf{g}_{b,y}^b(-) - \dot{\omega}_{ib,z}^b l_{rb,x}^b) + 2f_{ib,y}^b - \omega_{ib,z}^b(f_{ib,x}^b\tau_i + 2\mathbf{g}_{b,x}^b(-)\tau_i + 2v_{er,x}^r(-))] \\ \omega_{ib,y}^b & \approx \frac{\omega_{ib,z}^b f_{ib,y}^b}{f_{ib,z}^b} - \frac{\mathbf{g}_{b,y}^b(-)f_{ib,y}^b + \mathbf{g}_{b,z}^b(-)f_{ib,z}^b + f_{ib,y}^{b^2} + f_{ib,z}^{b^2}}{f_{ib,z}^b \left(\frac{1}{2}f_{ib,x}^b\tau_i + \mathbf{g}_{b,x}^b(-)\tau_i + v_{er,x}^r(-) \right)} \quad \begin{matrix} v_{er,x}^r(-) \geq g\tau_i \\ v_{er,x}^r(-) < g\tau_i \end{matrix}, \end{aligned} \quad (\text{E.61})$$

or, as attitude increments,

$$\alpha_{ib,x}^b \approx \frac{1}{f_{ib,z}^b} \left[2(g_{b,y}^b(-) - \dot{\omega}_{ib,z}^b l_{rb,x}^b) + 2f_{ib,y}^b - \alpha_{ib,z}^b (f_{ib,x}^b + 2g_{b,x}^b(-) + 2v_{er,x}^r(-)/\tau_i) \right]$$

$$\alpha_{ib,y}^b \approx \frac{\alpha_{ib,z}^b f_{ib,y}^b}{f_{ib,z}^b} - \frac{g_{b,y}^b(-) f_{ib,y}^b + g_{b,z}^b(-) f_{ib,z}^b + f_{ib,y}^{b^2} + f_{ib,z}^{b^2}}{f_{ib,z}^b \left(\frac{1}{2} f_{ib,x}^b + g_{b,x}^b(-) + v_{er,x}^r(-)/\tau_i \right)} \quad \begin{matrix} v_{er,x}^r(-) \geq g\tau_i \\ 0 \\ v_{er,x}^r(-) < g\tau_i \end{matrix}, \quad (\text{E.62})$$

noting that the condition on $v_{er,x}^r(-)$ is to prevent a potential singularity producing erroneously large values of the y-axis angular rate or attitude increment. The approximation $v_{er,x}^r(-) \approx v_{eb,x}^b(-)$ can typically be made.

These pseudo-measurements cannot be determined accurately over typical IMU measurement intervals of 20 ms or less. This is because small errors in the assumed motion constraints due to tire sideslip and the vehicle's suspension lead to large errors in the angular rate pseudo-measurements. These angular rate errors are proportional to the square of the update frequency. Useful pseudo-measurements can be obtained by increasing the measurement interval, τ_i , to 100 ms or more, averaging the IMU measurements over this interval. Note that better performance is obtained by retaining the original IMU update rate for the pseudo-measurements and performing the averaging over a moving window [22].

References

- [1] Waters, R. L., et al., "Factors Influencing the Noise Floor and Stability of a Time Domain Switched Inertial Device," *Proc. IEEE/ION PLANS*, Myrtle Beach, SC, April 2012, pp. 1099–1105.
- [2] Jekeli, C., "Navigation Error Analysis of Atom Interferometer Inertial Sensor," *Navigation: JION*, Vol. 52, No. 1, 2005, pp. 1–14.
- [3] Stockton, J. K., K. Takase, and M. A. Kasevich, "Absolute Geodetic Rotation Measurement Using Atom Interferometry," *Physical Review Letters*, Vol. 107, No. 13, 2011, Article ID 133001.
- [4] McGuinness, H. J., A. K. Rakholia, and G. W. Biedermann, "High Data-Rate Atom Interferometer for Measuring Acceleration," *Applied Physics Letters*, Vol. 100, 2012, Article ID 011106.
- [5] Butts, D. L., *Light Pulse Atom Interferometry at Short Interrogation Times for Inertial Navigation*, PhD Thesis, Massachusetts Institute of Technology, 2011.
- [6] Brown, D., et al., "Atom Interferometric Gravity Sensor System," *Proc. IEEE/ION PLANS*, Myrtle Beach, SC, April 2012, pp. 30–37.
- [7] Sorg, H. W., "From Serson to Draper—Two Centuries of Gyroscopic Development," *Navigation: JION*, Vol. 23, No. 4, 1976, pp. 313–323.
- [8] Titterton, D. H., and J. L. Weston, *Strapdown Inertial Navigation Technology*, 2nd ed., Stevenage, UK: IEE, 2004.
- [9] Lawrence, A., *Modern Inertial Technology*, 2nd ed., New York: Springer-Verlag, 2001.
- [10] Kayton, M., and W. G. Wing, "Attitude and Heading References," In *Avionics Navigation Systems*, 2nd ed., M. Kayton and W. R. Fried, (eds.), New York: Wiley, 1997, pp. 426–448.
- [11] Williams, T., et al., "Using an Accelerometer Configuration to Improve the Performance of a MEMS IMU: Feasibility Study with a Pedestrian Navigation Application," *Proc. ION GNSS 2009*, Savannah, GA, September 2009, pp. 3049–3063.
- [12] Edwan, E., S. Knedlik, and O. Loffeld, "Constrained Angular Motion Estimation in a Gyro-Free IMU," *IEEE Transactions on Aerospace and Electronic Systems*, Vol. 47, No. 1, 2011, pp. 596–610.
- [13] Williams, C. et al., "En Route Aids," in *Radio Aids to Civil Aviation*, R. F. Hansford, (ed), London, UK: Heywood & Company, 1960, pp. 164–311.
- [14] Tazartes, D. A., M. Kayton, and J. G. Mark, "Inertial Navigation," In *Avionics Navigation Systems*, Second Edition, pp. 313–392, M. Kayton and W. R. Fried (eds.), New York: Wiley, 1997.

- [15] Farrell, J. L., *Integrated Aircraft Navigation*, New York: Academic Press, 1976.
- [16] Collinson, R. P. G., “Inertial Navigation,” in *Navigation Systems*, G. E. Beck, (ed), London, UK: Van Nostrand Reinhold, 1971, pp. 207–255.
- [17] Jekeli, C., *Inertial Navigation Systems with Geodetic Applications*, Berlin, Germany: de Gruyter, 2000.
- [18] Kuipers, J. B., *Quaternions and Rotation Sequences*, Princeton, NJ: Princeton University Press, 1999.
- [19] Farrell, J. A., *Aided Navigation: GPS with High Rate Sensors*, New York: McGraw Hill, 2008.
- [20] Grewal, M. S., L. R. Weill, and A. P. Andrews, *Global Positioning Systems, Inertial Navigation, and Integration*, 2nd ed., New York: Wiley, 2007.
- [21] Groves, P. D., “Principles of Integrated Navigation,” Course Notes, QinetiQ Ltd., 2002.
- [22] Wang, B., M. Petovello, and P. D. Groves, private communications between University of Calgary and University College London, 2011-12.